Characterization of Fragmented Ultrahigh-Energy Heavy Ion Beam and Its Effects on Electronics Single-Event Effect Testing

Mario Sacristán Barbero, *Member, IEEE*, Ivan Slipukhin, Matteo Cecchetto, Daniel Prelipcean, Ygor Aguiar, Kacper Bilko, Natalia Emriskova, Andreas Waets, Andrea Coronetti, *Member, IEEE*, Maria Kastriotou, Carlo Cazzaniga, Torran Dodd, Frédéric Saigné, Vincent Pouget, *Member, IEEE*, and Rubén García Alía, *Member, IEEE*

Abstract— Ultrahigh-energy (UHE) (>5 GeV/n) heavy ion beams exhibit different properties when compared to standard and high-energy ion beams. Most notably, fragmentation is a fundamental feature of the beam that may have important implications for electronics testing given the ultrahigh energies and, hence, ranges, preserved by the fragments. In this work, both the primary lead ion beam, available in the Conseil Européen pour la Recherche Nucléaire (CERN) north area (NA), and its fragments are characterized by means of solid-state detectors. This input is later used to improve the measurements of single-event effects (SEEs) in commercial components with this beam. Moreover, the energy deposition distribution in the solid-state detectors is compared to that obtained with Monte Carlo simulations.

Index Terms— Beam fragmentation, FLUktuierende KAskade (FLUKA), heavy-ion beam, Monte Carlo simulations, RADiation facility Network for the EXploration of effects for indusTry and research (RADNEXT), single-event effects (SEEs), solid-state silicon detectors, super proton synchrotron (SPS) north area (NA), static random access memory (SRAM) memories, ultrahigh-energy (UHE) beam.

I. INTRODUCTION

THE interaction of high-energy ions with matter is of key importance for radiation environments and effects. Both space, where highly energetic ions are present as galactic cosmic rays (GCRs), and high-energy accelerators, where ions are accelerated in the scope of fixed-target and collider physics programs [1] are environments containing these particles. Single-event effect (SEE) testing with standard energy (SE, E < 10 MeV/n) and high-energy

(HE, 10 MeV/n < E < 100 MeV/n) ions is key in most of the radiation hardness assurance (RHA) procedures and shows a number of challenges such as the need of sample preparation, testing under vacuum, linear energy transfer (LET) variability along the sample, and limited availability of the facilities.

One alternative is increasing the ion energy, reaching the very-high-energy regime (VHE, 100 MeV/n < E <5 GeV/n) and, consequently, reaching larger ion ranges and more stable energies across the samples. As the ion range increases, the probability of the particle undergoing an inelastic collision increases accordingly and beam fragmentation may become a noticeable effect. This is a dominant phenomenon in the ultrahigh energy (UHE), (E > 5 GeV/n) range, where the reaction fragments preserve the same kinetic energy per nucleon and may be transported together with the primary beam. While SEE testing with UHE ions may be less interesting, due to the reduced LET and the impossibility to modify the primary energy, it allows studying in detail the beam fragmentation and how it can impact electronics testing.

The topic of using VHE and UHE ions for SEE studies was covered in [2], [3], [4], and [5], profiting from former VHE and UHE ion runs at the Conseil Européen pour la Recherche Nucléaire (CERN). In these, the effect of beam attenuation and fragmentation because of testing several layers in parallel is described, with a focus on how the SEE statistics can vary. Besides, other work [6] has shown that beam fragments can be useful to generate an LET distribution able to mimic that of the GCR in space, hence useful for testing in a realistic and comparable way.

While beam fragmentation can be a consequence of bulk materials placed in the beam line or parallel testing of multiple boards in a UHE beam, some amount of fragmentation can appear as well in the beam line as a consequence of collimators, beam windows, and transport in air. In this article, we analyze, through a combination of measurements and simulations, both the intrinsic fragmentation existent in the primary beam and secondary field of fragments created by a bulk fragmenter. This is studied for different material thicknesses and at different angles with respect to the primary beam. Several detectors and electronic components extensively calibrated and used in the frame of the Radiation to Electronics (R2E) project at CERN [7] and the Science and Technology Facilities Council (STFC) [8] were used to that aim.

Thanks to the characterization of the primary beam intensity and composition, single-event upset (SEE) measurements
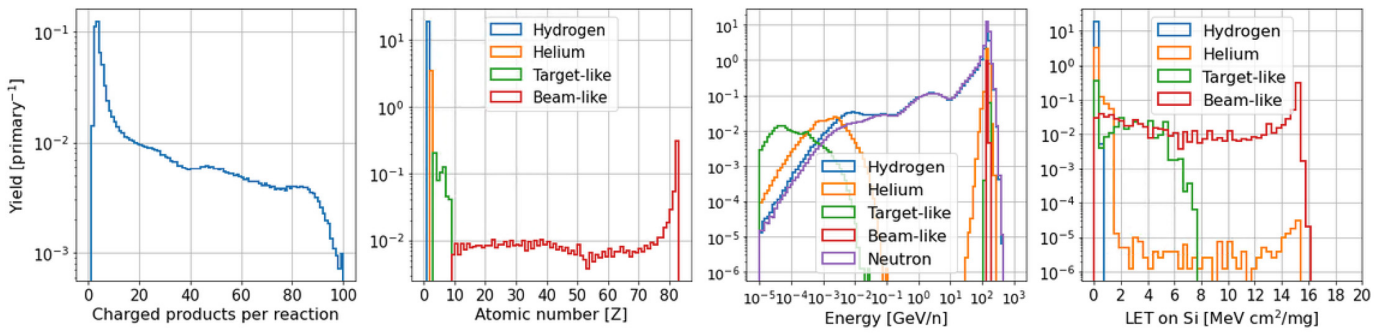
Fig. 1. Total number of products per nuclear reaction (1st), their atomic number (2nd), kinetic energy (3rd), and unrestricted LET on silicon (4th). Normalized per primary ion (^{208}Pb at 150 GeV/n) impinging on PMMA (composed by hydrogen, carbon, and oxygen).

could be performed and compared with more conventional heavy ion data for a few commercial references. The role and contribution of fragments were studied and corrected so that cross sections can be properly compared. Such measurements are representative of applications in which UHE ion beams interact with relatively thick shielding layers, resulting in a secondary radiation field whose characterization is essential in order to adequately assess and mitigate its possible effects on electronics.

By comparing measurements and simulations, this work assesses the suitability of the FLUktuierende KAskade (FLUKA), Monte Carlo radiation–matter interaction and transport code [9], [10], [11], [12] to describe the environment resulting from the interactions of high-energy ions with a variety of material thicknesses, which can be of relevance to radiation effects in space and high-energy accelerators.

II. SPS NA UHE BEAMS

The heavy-ion program at CERN takes place during the last weeks of operation every year. After studies with other ion species in past years, the current ion choice is ^{208}Pb 150 GeV/n, which can be used at the super proton synchrotron (SPS) north area (NA) facility for electronics testing [13], [14]. The NA is a general-purpose beam test facility hosting several fixed-target experiments. In particular, the measurements described in this article took place in line H8, experimental point 138, which hosts a versatile open area where the beam line can be customized by placing several detector layers and passive elements such as fragmenters. Furthermore, the NA belongs to the RADiation facility Network for the EXploration of effects for indusTry and research (RADNEXT) facility network [15].

The beam provided at the NA is a pulsed beam with an approximate duration of 9 s, and the beam repetition rate is typically between 1 and 2 spills per minute, depending on the combined needs of the ongoing heavy ion experiments.

The stopping range in silicon would be larger than 8 m if nuclear interactions were not considered, based on FLUKA calculations. Precisely, the inelastic scattering length (mean distance between two inelastic collisions) for this beam in silicon is approximately 5 cm, slowly varying as a function of the energy. This renders impossible in practice a noticeable variation of kinetic energy through electromagnetic stopping. Moreover, as already discussed in [2] and [3] and depicted in Fig. 1, the kinetic energy per nucleon of the ions is preserved by beam fragments after the collisions and can be

transported downstream, impacting the samples under test. Thanks to FLUKA, the interactions of the primary particles with a raw piece of material of the fragmenter can be studied. The distribution of product ions created from inelastic interactions at such high energies is plotted in Fig. 1. As shown in the leftmost graph, the main reaction happening is the primary ion spallation in which this becomes lighter and releases a few light fragments (typically neutrons, protons, and hydrogen/helium isotopes). In particular, the dominant cases are when the lead ion is either fully split into light particles or when the primary suffers a small reduction in charge/mass numbers. Beam fission or heavier products than primary ions are totally suppressed. The rest of the graphs allow classifying the reaction products into three categories given their atomic number and energy/LET. These types are given as follows.

1) *Beam-Like Fragments:* Ions carrying kinetic energies per nucleon close to the primary one (150 GeV/n).
2) *Target-Like Fragments:* Ions with atomic numbers equal or close to those present in the fragmenter and kinetic energy ranging from keV/n to MeV/n.
3) *Hydrogen and Helium Fragments:* Isotopes with $Z = 1$ and $Z = 2$ show a certain degree of dispersion in energies and are produced both from the primary beam ions and the fragmenter material.

As to what concerns the LET, as already shown in [16], the energies of the delta rays can be large enough to deposit the energy far from the volume of interest. In that sense, despite showing the unrestricted LET value (i.e., ion stopping power per unit density) on silicon in Fig. 1, in what follows equivalent LET restricted to 1-μm^3 cubic volume, 8 MeV cm^2/mg will be used for the SEE calculations. In Fig. 2, the equivalent LET for different cubes of a given size is depicted, showing the variability as a function of the size. Thus, the value to be used in SEE calculations is 8 MeV cm^2/mg.

III. EXPERIMENTAL SETUP

The monitoring of the beam is typically performed by means of scintillators (XSCI) and delay wire chambers (XDWC) to determine the total number of counts and beam spatial width (horizontal and vertical) on a spill-by-spill basis, respectively. Nevertheless, these instruments were used only for reduced periods of time, relying for most of the irradiation on our dedicated R2E detectors.

1) A 300-μm-thick silicon solid-state detector with 2×2 cm^2 sensitive area was used to monitor the intensity of the beam and its temporal structure [16], [17].
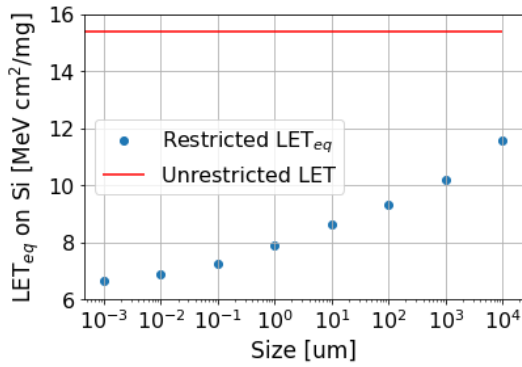
Fig. 2. Restricted LET (blue) on silicon of ^{208}Pb at 150 GeV/n for different cubic volumes of given edge length and unrestricted LET on silicon (red).

Its signal is augmented with a 20-dB current-sense amplifier Cividec C1-HV to be later directly sampled with a digitizer. The energy resolution was determined to be <1% in previous calibrations with heavy ions.

2) A European Space Agency (ESA) single-event upset (SEU) Monitor Atmel chip was used to measure the beam size and homogeneity over its 1.9×1.9 cm^2 sensitive surface [18], [19]. Its software allows identifying the number and position in space of the bit-flips between each read/write cycle.

3) Custom-made board consisting of a 4×4 grid of static random access memory (SRAM) memories (23LC1024) and a total area of 4×5 cm^2, allowing to complete and compare beam spatial width and homogeneity [20].

4) A TimePix3 detector, part of the TimePix detector family and designed by the Medipix collaboration, is a pixel detector consisting of a sensor chip with a matrix of 256×256 pixels, 55×55 μm^2 each. It is designed as a timing measurement chip that enables determining the deposited charge, using the time over threshold (ToT) technique [21], [22], [23].

5) Radio-photoluminescence (RPL) glass dosimeters are already used as a high-level radiation monitor in the mixed radiation fields observed in CERN's accelerator environment [24].

All these instruments and detectors have been widely characterized in many fields, including heavy ions from standard energies to UHE. Besides, during certain runs, a block of polymethyl methacrylate (PMMA) of different thicknesses (4, 8, or 12 cm) was placed upstream to enhance the beam fragmentation. These values were deliberately selected since they represent approximately λ, 2λ, and 3λ, where λ is the inelastic length in the material. The fragment field was then measured with the instruments at different angles with respect to the primary beam by performing transversal translations along the Y-axis. The aim is to observe how the composition of the beam in terms of energy deposition varies when going decentered from the primary beam. In Fig. 3, the whole experimental setup is depicted. Right in front of the beam window, a set of beam instruments (scintillator and delay wire chamber) would be present for calibration purposes. The first layer was reserved for the fragmenter, which was used during specific runs only. Finally, a moveable table with several layers of detectors is placed. The first layer was reserved for SEE testing of the different samples (SRAMs
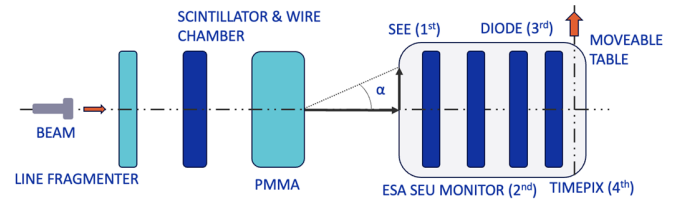

Fig. 3. Schematic description of the setup, showing the main elements of the different configurations.
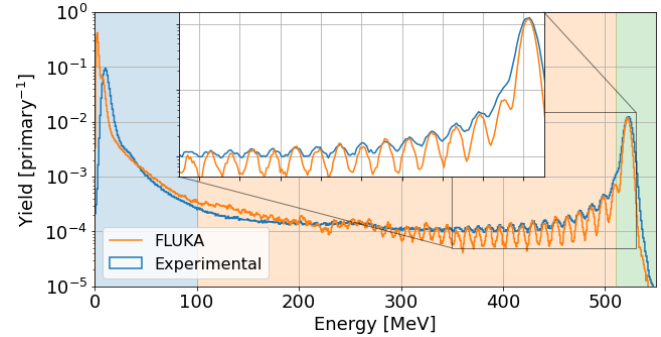

Fig. 4. Experimental deposited energy of the primary beam events in the silicon diode (blue) and the simulation of the field with FLUKA (orange). In the background, the three types of beam elements are colored: primary ions in green, heavy ion fragments in orange, and the rest of the low-energy events in blue. Experimental peaks are only ×1.3 (or less) larger than simulated ones.

and MOSFET), given that the primary ion flux is higher than in the layers downstream. In the second and third positions, the ESA SEU Monitor and the silicon diode would be placed constantly for dosimetry purposes. Finally, the TimePix3 and an array of RPLs could be found. Note that in the simulations, a virtual element, beam line fragmenter, was used to increase the default level of fragments and match it to that found in the facility, accounting for the elements (vacuum windows, beam instruments, collimators, and air) present in the beam line but not explicitly included in the simulation.

IV. CHARACTERIZATION OF PRIMARY UHE HEAVY ION BEAM

As mentioned above, the silicon diode allowed monitoring the beam flux and composition by counting the number of events and by discriminating the particle deposited energy. The latter is depicted in Fig. 4. The energy distribution can be divided into three main regions: the main primary ion peak, depositing energies larger than 510 MeV, the fragments plateau between 510 and 100 MeV, and a low-energy peak for events depositing less than 100 MeV. The justification for this classification is mainly qualitative, given that the maximum LET is that of the primary ion, and every fragment features a smaller LET, thus depositing less energy. The cumulative flux values can be found in Table I.

Moreover, since the kinetic energy per nucleon of the fragments is preserved, the change in the LET is a direct consequence of the Z number reduction. Since LET is roughly proportional to Z^2, small changes in Z translate into large variations in the LET and, thus, in the deposited energy. The result is a peak distribution in the deposited energy, which can be resolved by the silicon detector. This is true only for heavy fragments close to the primary ion since, for smaller Z, the separation becomes smaller than the detector resolution.
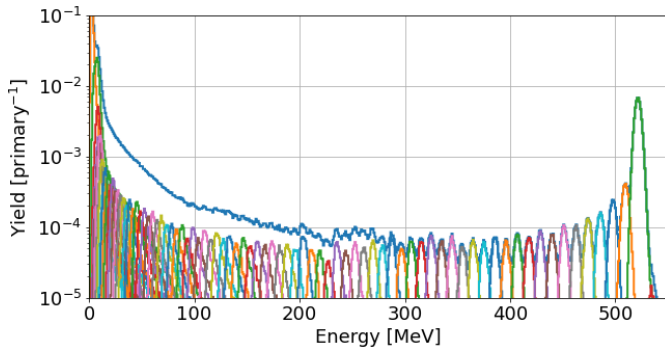
Fig. 5. Distribution of events as a function of deposited energy. Each color refers to a different Z, being this one of the heaviest ion fragment for each event. The largest green peak on the right is the primary lead ions, and every peak on the left follows a regression in Z.

TABLE I
PRIMARY SPS NA BEAM COMPOSITION

Particle	Deposited energy [MeV]	Flux [particle/cm^2/spill]
Primary ion	$E > 510$	684
Heavy fragments	$100 < E < 510$	310
Light fragments	$E < 100$	4100

As classified in Fig. 1 as a function of the deposited energy in a silicon detector.

The deposited energy was simulated with FLUKA, using a configuration with a 2-cm-thick beam line fragmenter made of beryllium and no bulk PMMA fragmenter. A moderate number of fragments are expected to come from the ESA SEU Monitor layer placed right in front of the silicon diode. The result is shown in Fig. 4, where an x-axis proportional fit is applied to match the experimental results. The detector acquisition line experienced reflections and losses that reduced the magnitude of the acquired signal, hence reducing the value of deposited energy, which is larger in the Monte Carlo simulations. Nevertheless, due to the perfect match of the fragment peaks in the deposited energy, the fit is straightforward. In Fig. 5, the deposited energy of every event is plotted with a different color as a function of the Z atomic number of the heaviest fragment. It can be seen how indeed every peak corresponds to a different Z and how, at approximately 100 MeV, the peaks overlay each other. In this way, we can define three beam fluxes, for primary ions, heavy fragments, and low-energy events. It is important to stress that no fragmenter material was introduced for this measurement, so these background fragments are present inevitably due to the beam line configuration.

As to what concerns the beam spatial width and homogeneity, the ESA SEU Monitor data were compared to those from the delay wire chamber. First, as shown in Fig. 6, the beam shape detected by the wire chamber is approximately Gaussian in both the X- and Y-directions, on the order of 3 and 4 cm (2σ), respectively. Thus, the good alignment with the beam, ensured by the ESA Monitor, and the active area of the detectors, typically 4 cm^2, allows capturing the central part of the beam, which is assumed to be reasonably flat.

Besides, thanks to the transversal movements that can be performed on the setup and the spatial resolution of the SRAM grid, the beamwidth in the X-axis can be resolved and compared, as shown in Fig. 6, confirming the 3-cm beamwidth (2σ) in that direction.
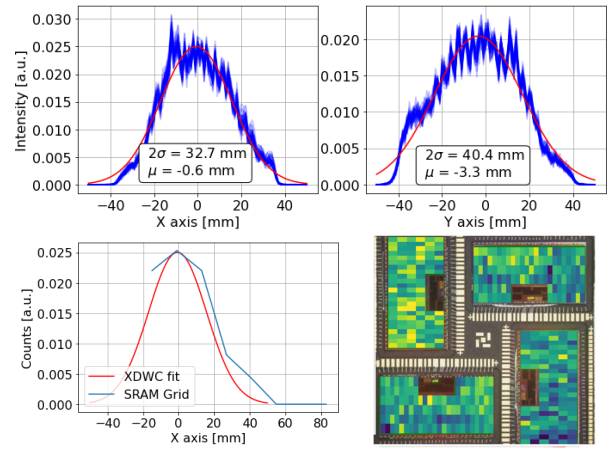

Fig. 6. Measurement of the X and Y spatial profile of XWDC beam detectors and the measured beamwidth (top). Relative Gaussian fit error is 4% for σ and 25% for μ. Comparison of spatial beamwidth in the X-axis of facility instrument XDWC and SRAM grid (bottom left). Distribution of SEUs in the ESA SEU Monitor chip.
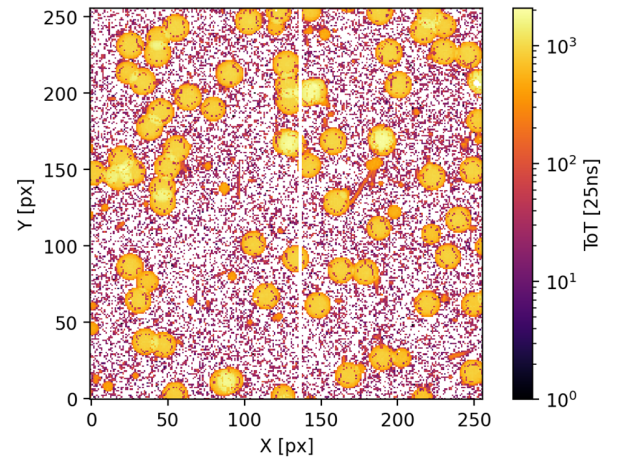

Fig. 7. Timepix3 Radiation Monitor pixel matrix readout for a 1-s time window during a run with no fragmenter.

Finally, the Timepix3 radiation monitor was also used with a twofold purpose. First, the instrument was used to characterize the beam, taking advantage of its excellent time resolution and its potential for energy deposition studies. As an example, a view of the 1-s time integrated readout of the pixel matrix for the primary beam without any fragmenter is shown in Fig. 7, where one can observe the heavy ions (big blobs due to charge sharing to adjacent pixels), as well as smaller blobs (heavy fragments of different charge) and individual pixel hits (lightest particles). The associated flux rate for the duration of this run is shown in Fig. 8, displaying the time structure of the beam with spills of about 10 s, repeated every minute.

The latter scope was to investigate the energy calibration analysis for a Timepix3 sensor, noting the known saturation effect at large energy depositions per pixel [25], [26], called the "volcano effect." It causes substantially lowered measurement of input charges in a pixel. It is a caldera-like hollowing out of the measured energy deposition in the center of a cluster and a net loss of total measured energy deposition with respect to what would be theoretically expected and is linked to design constraints in the readout chip. For this reason, the measured
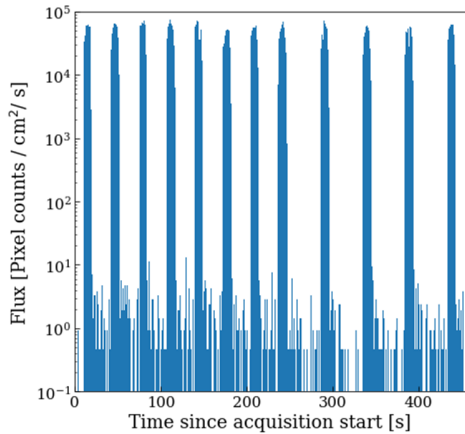
Fig. 8. Flux rate measured by the Timepix3 Radiation Monitor given in pixel hits (and not particles, which require clustering).

TABLE II
RELATIVE PRIMARY FLUX AS A FUNCTION OF FRAGMENTER THICKNESS

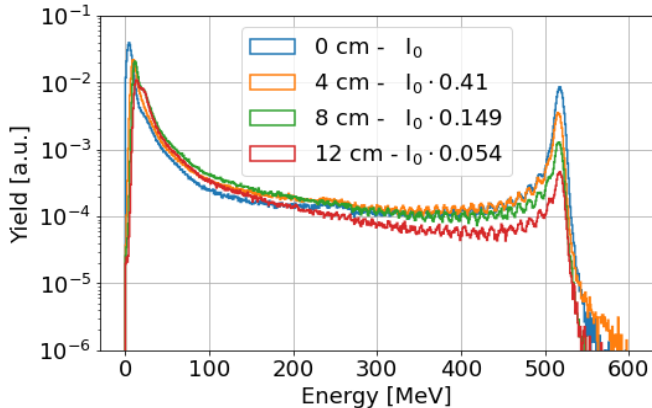| Thickness [cm]	Thickness [λ]	Analytical flux reduction	Experimental flux reduction
0	0	-	-
4	1	0.37	0.41
8	2	0.135	0.149
12	3	0.050	0.054

Fig. 9. Experimental distribution of events as a function of the deposited energy and the thickness of the PMMA fragmenter used. The peak of the primary ion beam is reduced coherently with the thickness.

energy spectra require more sophisticated postprocessing to correct for this saturation, which will be the scope of future publications.

Concerning the RPL placed along the beam line, in the position right behind the silicon diode, the post-test analysis determined the absorbed dose to be 2.0 Gy, which is in reasonable agreement with the dose provided by the simulations, 2.3 Gy.

V. FIELD OF FRAGMENTS OF UHE HEAVY ION BEAM

Once having measured the primary beam properties without any fragmenter, different layers of PMMA were put between the beam output and the detectors. As shown in Fig. 9, the primary ion peak of the energy distribution progressively decreases due to the cumulative fragmentation in the beam.
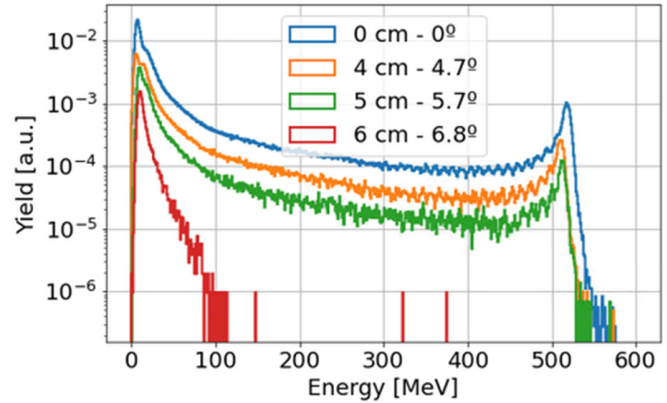

Fig. 10. Experimental distribution of events as a function of the deposited energy and the transversal distance of the detector with respect to the beam. Transversal angle assuming that detector is 50 cm far from the fragmenter. PMMA thickness is 8 cm.

The reduction is defined by the following relation:

$$I = I_0 e^{-\frac{d}{\lambda}} \qquad (1)$$

where I, I_0, d, and λ are the final and initial intensities, the material thickness, and the inelastic length in the material, respectively. The results match the expected values of 4, 8, and 12 cm in PMMA, in good agreement with the values shown in Table II. Similarly, the fragment plateau suffers additional fragmentation, further reducing the heavier components while keeping a relatively constant value for lighter fragments. Given that the light fragments are generated by the primary beam and they cannot suffer additional fragmentation, their amount remains almost constant. It is important to note that inelastic distance increases considerably as the atomic number Z is reduced.

During a final run with the 8-cm-thick fragmenter in the beam, the detectors were moved perpendicularly with respect to the beam line. The results in Fig. 10 show that the distribution remained identical in composition as long as the detector overlapped the beam size. As soon as the detector was fully off the beam, only lighter fragments were detected with the silicon diode. The interpretation of this is that heavy fragments exhibit no deflection with respect to the beam line due to the extreme momentum. Only the lightest fragments with the lowest Z values can deflect considerably to be detected in the beam halo.

VI. SEEs INDUCED BY UHE ION BEAM

A. Single-Event Upset

As a final step to understand the impact of fragments in SEE testing of commercial components, the beam is used to induce SEUs in two commercial memories previously characterized, the ISSI 40 nm (ISSI IS61WV204816BLL-10TLI, date code 1650) and Cypress 65 nm (CYPRESS CY62167GE30-45ZXI date code 1731) [28], together with the ESA SEU Monitor. The irradiation took place at normal incidence, 3.3-V bias voltage, and room temperature, while the read/write operation took place every minute, to match the pulse frequency, using a checkerboard pattern. In Fig. 11, the SEU cross sections for UHE heavy ions are plotted and compared to those found in other facilities with standard energies, namely, RADEF and Kernfysisch Versneller Instituut (KVI), which is
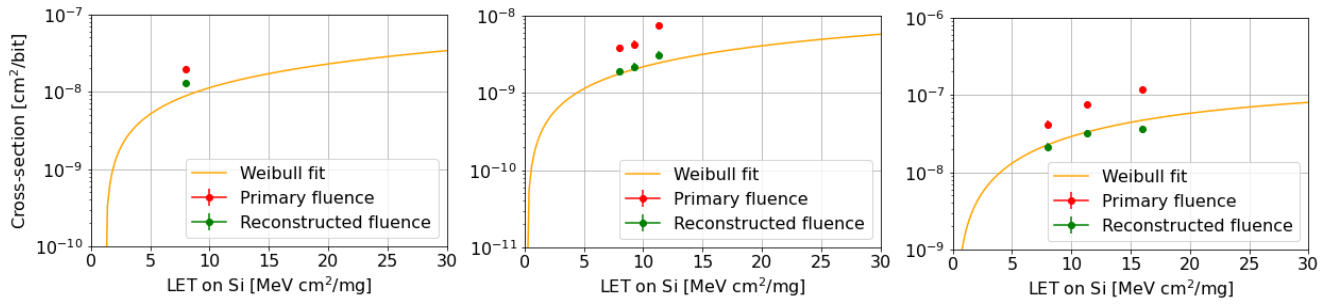
Fig. 11. SEU cross sections of ESA SEU Monitor (left), ISSI IS61WV204816BLL (center), and Cypress CY62167GE30 (right). Red points are the cross section retrieved by using the flux of primary ions provided by the silicon diode. Green values are obtained with (3), having weighted the differential fluence with the Weibull fit and including the beam difference between the two layers. Weibull fit follows the measurement with standard energy heavy ions. The three memories show the following tilt angles: ESA SEU Monitor 0°; ISSI 0°, 30°, and 45°; and Cypress 0°, 45°, and 60°. Effective LETs and fluences are corrected using the cosine rule as discussed in [27]. Error bars are set assuming a 95% confidence level in SEE statistics and 10% variation in fluence and are smaller than the markers. Primary fluence values are at least ×2 larger than the Weibull fit ones, while the ones with the reconstructed fluence are only ×1.3 larger or less.

calculated by (2), where SEE is the number of events and ϕ is the test fluence, following the SEE testing standards, and represented by their Weibull fit [26], [27]. In the case of using the primary beam flux provided by the silicon detector, it can be seen how the cross section is overestimated because of two reasons.

1) The number of primary ions measured by the silicon detector is not necessarily the same as the primary flux reaching the device under test.
2) The existence of heavy fragments with different LETs with respect to primary ions is still capable of inducing SEE

$$\sigma_{\text{Primary}} = \frac{\text{SEE}}{\phi}. \quad (2)$$

Fortunately, due to the full characterization of these devices at several facilities, the Weibull fit as a function of the LET is known and the limitations can be overcome with the following approximations.

1) The primary beam attenuation shall be calculated, as addressed in [2]. In the case of simple layers, (1) can be used to approximate this amount. For more complex geometries, Monte Carlo simulations can provide insight into how the beam intensity and composition vary in any test position. In this way, an attenuation factor as a function of the LET, $\alpha(\text{LET})$, can be extracted. In the case of this article, the simulations using the schematic of Fig. 3 showed that the variability is only important for the primary beam intensity, having an attenuation of 40%, given the intermediate layers between the SEE sample and the silicon diode positions.
2) Because of the UHE kept by both the primary ions and the fragments, the energy and LET can be assumed constant along the sample. This means that the deposited energy of every fragment species is proportional to the LET. Hence, the distribution provided by the silicon detector can be seen precisely as an LET distribution, whose response in the sample can be weighted by the Weibull function already known.

Because of this, we can reformulate the cross section definition for a reconstructed UHE fragmented beam

$$\sigma_{\text{Frag}} = \frac{\text{SEE}}{\int \frac{d\phi}{d\text{LET}} \frac{\sigma_W(\text{LET})}{\sigma_{W,Pb}} \alpha(\text{LET}) d\text{LET}} \quad (3)$$

TABLE III
SEL CROSS SECTION UPPER LIMIT

Memory	RADEF 7.2 MeV cm²/mg	CERN North Area 8 MeV cm²/mg
Samsung K6R4016V1D	1.0×10⁻⁶ cm²	< 1.4×10⁻⁵ cm²
Alliance AS7C34098A	2.0×10⁻⁶ cm²	< 1.4×10⁻⁵ cm²

where $(d\phi/d\text{LET})$ is the differential flux as provided by the silicon diode, $(\sigma_W(\text{LET})/\sigma_{W,Pb})$ is the Weibull cross section of the sample, normalized by the primary beam cross section, and $\alpha(\text{LET})$ is the attenuation factor from Monte Carlo simulations accounting for the ratio of primaries actually reaching the sensitive region over the initial presumed amount.

As can be observed in Fig. 11, the initial cross section overestimation from the standard definition is mitigated with the corrected flux definition for the three SRAM memories.

B. Single-Event Latch-Up

Two single-event latch-up (SEL)-susceptible memories were tested. Unfortunately, due to beam time constraints, high fluence could not be reached and no SEL was found, allowing only to set a cross section upper limit, which is compatible with other standard energy ions used in the past. In Table III, the values are listed. Furthermore, the LET cross section threshold is found very close to the primary beam LET, so the impact of fragments is assumed as negligible.

C. Single-Event Burn-Out

Finally, the power MOSFET reference IRFB4105ZPBF (55-V maximum drain voltage) was tested with a similar setup as the one described in [29]. Precisely, the reference was tested at the NA in 2018 and at KVI in 2019, and the data are plotted in Fig. 12 for comparison. The cross section results for different voltages seem to follow the same trend between the year 2018, also ²⁰⁸Pb at 150 GeV/n, and 2022 for the NA facility. On the contrary, these results disagree with cross section for the same device using standard heavy ion energies at comparable LET (⁴⁰Ar, 14 MeV/n, LET 8.5 MeV cm²/mg at KVI). Two main differences emerge.
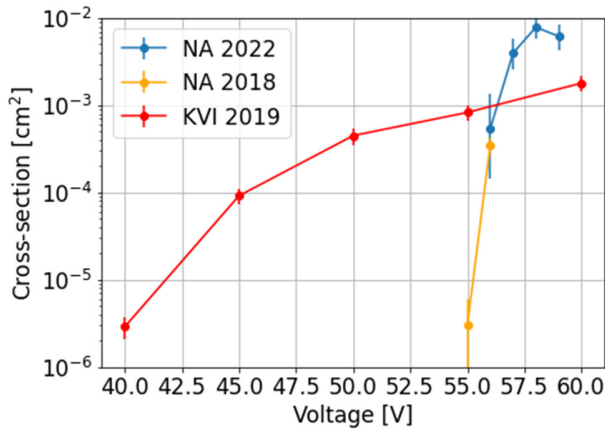
Fig. 12. SEB cross section at LET 8 MeV cm^2/mg. Different threshold and saturation values are found for standard and ultrahigh-energy error bars are set assuming a 95% confidence level in SEE statistics and a 10% variation in fluence.

1) *Different Saturation Cross Section at High Voltage:* In a similar way as for the SEUs in SRAM memories, simply using the primary beam flux primary ions leads to a cross section overestimation. However, for this device, a characterization as a function of LET does not exist, so the contribution of the fragments cannot be calculated. Most probably that is the reason for the different values.

2) *Different Voltage Threshold for Single-Event Burn-Out (SEB):* Having similar LET, at the NA, it is needed to bias sample at the maximum voltage (55 V) to detect SEBs; on the contrary, these events appeared at KVI at 40 V. While more research may be needed to clarify this, this might indicate a potential SEE behavior for beams with similar LET but different energy.

VII. POSSIBLE IMPLICATIONS IN SEE TESTING

As shown in the previous section, the presence of beam fragments together with the primary beam may cause an overestimation of the SEE cross section if these are not considered properly. Nevertheless, this challenge can be overcome by both.

1) Using a facility dosimeter that allows fragment discrimination, as described in this article with the silicon diode. The differential flux as a function of the LET can be thus weighted with the Weibull calibration function of the sample when this one is available.

2) Building a realistic model of the setup that accounts for the material composition and geometries, allowing to identify the primary beam attenuation between the positions of the dosimeter and the device under test.

When these two conditions are met, the ion beam intensity can be reconstructed as shown in (3).

Furthermore, the impact of light fragments, namely, neutrons and hydrogen isotopes, also deserves a specific comment. Despite their very low (or zero) LET, they would still be capable of inducing SEEs through inelastic reactions within the sample under test. As shown in [30], the indirect SEU saturation cross section for the three SRAMs under study is at least five orders of magnitude lower than the direct SEU cross

TABLE IV
SEU DIRECT VERSUS INDIRECT CROSS SECTIONS

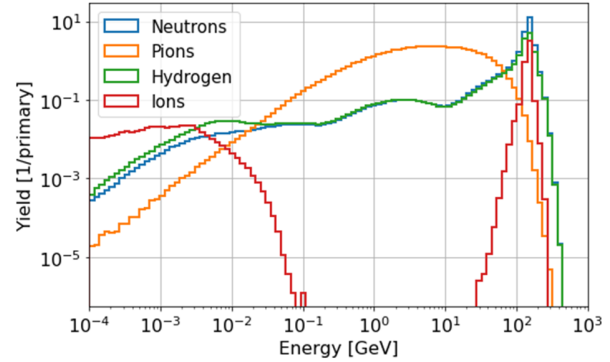| Memory	Pb direct [cm^2/bit]	Neutron indirect [cm^2/bit]	Pion indirect [cm^2/bit]
ESA SEU Monitor	8.8×10^{-9}	2.6×10^{-14}	5.5×10^{-14}
ISSI IS61WV2048	1.8×10^{-9}	1.4×10^{-14}	4.0×10^{-14}
Cypress CY62167GE30	2.3×10^{-8}	7.7×10^{-14}	---

Fig. 13. Energy distribution of reaction products of ^{208}Pb 150 GeV/n in PMMA. "Hydrogen" accounts for protons, deuterons, and tritons, while "Ions" include every isotope with a charge larger than 1. "Pions" include the positive, negative, and neutral types.

TABLE V
LIGHT FRAGMENT YIELD IN ^{208}Pb 150 GeV/n INELASTIC REACTIONS

Particle	Yield [1/primary]
Protons	18.8
Neutrons	29.8
Pions (all)	58.1

section for the primary ion LET. Similarly, in [31], the cross section values for indirect pion SEU and SEL are found to be in the same order of magnitude as for the events generated by other hadrons. These values are summarized in Table IV.

Hence, as a qualitative analysis, indirect SEUs are expected to compete with direct ionization SEUs once the cumulated hadron flux dominates the ion flux by five orders of magnitude, to compensate the smaller cross section. As an example, Fig. 13 shows the number of light fragments (protons, neutrons, and pions) compared to ion fragments as they are created in primary ion inelastic reactions in the fragmenter. As discussed in Fig. 1, many of the inelastic reactions happening imply full spallation of the primary particle, hence producing a large number of protons, neutrons, and pions.

A legitimate question would be at what point the light fragments can pose a risk in terms of SEE calculation due to a mixture of direct ion SEEs and indirect neutron/pion SEEs. This question is highly dependent on geometry and materials, but some toy model calculations suggest the following.

1) As can be seen in Table V, in every primary inelastic reaction in the fragmenter, approximately 100 light fragments are produced.

2) Since the indirect SEE cross section is approximately five orders of magnitude lower than that for the direct SEE, the required light fragment flux should be larger

by the same amount. Hence, with the simple probability of an inelastic reaction

$$I_{f,\text{ion}} = I_{0,\text{ion}} e^{-\frac{d}{\lambda}} I_{f,\text{hadron}} = 100\left(I_{0,\text{ion}} - I_{f,\text{ion}}\right) \quad (4)$$

$$\frac{I_{f,\text{hadron}}}{I_{f,\text{ion}}} > 10^5 \rightarrow d > 7 \quad (5)$$

where $I_{f,\text{ion}}$, $I_{f,\text{hadron}}$, and $I_{0,\text{ion}}$ refer to final ion flux, final hadron flux, and initial ion flux, respectively.

Hence, in this model, indirect SEUs would compete with direct SEUs after a fragmenter of seven times the inelastic length, in the case of PMMA, 28 cm.

VIII. Conclusion and Outlook

Electronics SEE testing with UHE ions has a number of advantages, such as testing complex 3-D designs, parallel board testing, and continuous LET along the device. However, beam fragmentation is the main phenomenon in these beams and needs to be addressed and characterized to prevent overestimation/underestimation of the flux and its potential impact on the SEE cross section calculation.

Moderate amount of fragmentation can typically be found in UHE beams, particularly at beam lines with a number of instruments, beam windows, and air before reaching the device under test. To this aim, the primary ion beam at the SPS NA has been measured with silicon-based detectors, establishing its intensity, profile, and composition. The fragment abundance has been measured and compared to that retrieved in FLUKA Monte Carlo simulations, showing an equivalent fragmenter length of 2 cm. Moreover, it has been shown how the initially overestimated cross section values can be corrected for the cases when the Weibull fit is already known, together with the effective beam composition.

As to what concerns the SEE cross sections from the UHE beam, SEU and SEL values are in good agreement with those found with standard energy ions, while that is not the case for SEB cross section, pointing to a potential role of not only the LET but also the energy in these events. Finally, a simple model from Monte Carlo simulations suggests that very strong fragmentation is needed so that indirect SEEs from hadrons overcome the direct SEEs from ions, being required on the order of seven times the inelastic length of fragmenter material. Further research is required to confirm this value.

References

[1] R. G. Alía et al., "Heavy ion energy deposition and SEE intercomparison within the RADNEXT irradiation facility network," *IEEE Trans. Nucl. Sci.*, vol. 70, no. 8, pp. 1596–1605, Mar. 2023.

[2] M. Kastriotou et al., "Single event effect testing with ultrahigh energy heavy ion beams," *IEEE Trans. Nucl. Sci.*, vol. 67, no. 1, pp. 63–70, Jan. 2020.

[3] R. G. Alía et al., "Ultraenergetic heavy-ion beams in the CERN accelerator complex for radiation effects testing," *IEEE Trans. Nucl. Sci.*, vol. 66, no. 1, pp. 458–465, Jan. 2019.

[4] V. Wyrwoll et al., "Longitudinal direct ionization impact of heavy ions on see testing for ultrahigh energies," *IEEE Trans. Nucl. Sci.*, vol. 67, no. 7, pp. 1530–1539, Jul. 2020.

[5] V. Wyrwoll et al., "Heavy ion nuclear reaction impact on SEE testing: From standard to ultra-high energies," *IEEE Trans. Nucl. Sci.*, vol. 67, no. 7, pp. 1590–1598, Jul. 2020.

[6] R. G. Alía et al., "Fragmented high-energy heavy-ion beams for electronics testing," *IEEE Trans. Nucl. Sci.*, vol. 70, no. 4, pp. 486–495, Apr. 2023.

[7] *R2E Website*. Accessed: Jan. 9, 2024. [Online]. Available: https://r2e.web.cern.ch/

[8] *STFC Website*. Accessed: Jan. 9, 2024. [Online]. Available: https://www.ukri.org/councils/stfc/

[9] G. Battistoni et al., "Overview of the FLUKA code," *Ann. Nucl. Energy*, vol. 82, pp. 10–18, Aug. 2015.

[10] C. Ahdida et al., "New capabilities of the FLUKA multi-purpose code," *Frontiers Phys.*, vol. 9, Jan. 2022, Art. no. 788253.

[11] A. Fasso' et al., "The FLUKA code: Present applications and future developments," 2003, *arXiv:physics/0306162*.

[12] V. Vlachoudis, "FLAIR: A powerful but user-friendly graphical interface for FLUKA," in *Proc. Int. Conf. Math., Comput. Methods React. Phys. (MC2)*. New York, NY, USA: Saratoga Springs, May 2009, pp. 790–800.

[13] L. Gatignon, "Physics at the SPS," *Rev. Sci. Instrum.*, vol. 89, May 2018, Art. no. 052501.

[14] K. Bilko et al., "CERN super proton synchrotron radiation environment and related radiation hardness assurance implications," *IEEE Trans. Nucl. Sci.*, vol. 70, no. 8, pp. 1606–1615, Aug. 2023.

[15] *Radiation Facility Network for the Exploration of Effects for Industry and Research*. Accessed: Jan. 9, 2024. [Online]. Available: https://radnext.web.cern.ch/

[16] M. Bagatin et al., "Characterizing high-energy ion beams with PIPS detectors," *IEEE Trans. Nucl. Sci.*, vol. 67, no. 7, pp. 1421–1427, Jul. 2020.

[17] K. Bilko et al., "Silicon solid-state detectors for monitoring high-energy accelerator mixed field radiation environments," in *Proc. 21st Eur. Conf. Radiat. Its Effects Compon. Syst. (RADECS)*, Vienna, Austria, Sep. 2021, pp. 1–5.

[18] R. Harboe-Sorensen et al., "From the reference SEU monitor to the technology demonstration module on-board PROBA-II," *IEEE Trans. Nucl. Sci.*, vol. 55, no. 6, pp. 3082–3087, Dec. 2008.

[19] R. Harboe-Sorensen et al., "PROBA-II technology demonstration module in-flight data analysis," *IEEE Trans. Nucl. Sci.*, vol. 59, no. 4, pp. 1086–1091, Aug. 2012.

[20] L. Obermueller, C. Cazzaniga, S. Kulmiya, and C. D. Frost, "A fast neutron monitor based on single event effects in SRAMs using commercial off-the-shelf components," in *Proc. 18th Eur. Conf. Radiat. Effects Compon. Syst. (RADECS)*, Goteborg, Sweden, Sep. 2018, pp. 1–5.

[21] T. Poikela et al., "timepix3: A 65K channel hybrid pixel readout chip with simultaneous ToA/ToT and sparse readout," *J. Instrum.*, vol. 9, no. 5, May 2014, Art. no. C05013.

[22] N. A. Tehrani et al. (2015). *Calibration of Ultra-Thin Hybrid Pixel Detector Assemblies With Timepix Readout ASICs*. Accessed: Jan. 9, 2024. [Online]. Available: http://cds.cern.ch/record/2054922

[23] X. Llopart, R. Ballabriga, M. Campbell, L. Tlustos, and W. Wong, "Timepix, a 65k programmable pixel readout chip for arrival time, energy and/or photon counting measurements," *Nucl. Instrum. Methods Phys. Res. A, Accel. Spectrom. Detect. Assoc. Equip.*, vol. 581, nos. 1–2, pp. 485–494, Oct. 2007.

[24] D. Pramberger, Y. Q. Aguiar, J. Trummer, and H. Vincke, "Characterization of radio-photo-luminescence (RPL) dosimeters as radiation monitors in the CERN accelerator complex," *IEEE Trans. Nucl. Sci.*, vol. 69, no. 7, pp. 1618–1624, Jul. 2022.

[25] S. M. A. Al Azm et al., "Response of timepix detector with GaAs: Cr and Si sensor to heavy ions," *Phys. Particles Nuclei Lett.*, vol. 13, no. 3, pp. 363–369, May 2016.

[26] S. P. George et al., "Very high energy calibration of silicon timepix detectors," *J. Instrum.*, vol. 13, no. 11, Nov. 2018, Art. no. P11014.

[27] (2014). *Single Event Effects Test Method and Guidelines, ESCC Basic Specification 25100*. Accessed: Feb. 1, 2024. [Online]. Available: https://escies.org/specification/viewapppub?id=3095

[28] A. Coronetti et al., "SEU characterization of commercial and custom-designed SRAMs based on 90 nm technology and below," in *Proc. IEEE Radiat. Effects Data Workshop (Conjunct With NSREC)*, Santa Fe, NM, USA, Nov. 2020, pp. 1–8.

[29] P. Fernández-Martínez et al., "SEE testing on commercial power MOSFETs," in *Proc. 20th Eur. Conf. Radiat. Its Effects Compon. Syst. (RADECS)*, Toulouse, France, Oct. 2020, pp. 1–8.

[30] M. Cecchetto et al., "0.1–10 MeV neutron soft error rate in accelerator and atmospheric environments," *IEEE Trans. Nucl. Sci.*, vol. 68, no. 5, pp. 873–883, May 2021.

[31] A. Coronetti, "Relevance and guidelines of radiation effect testing beyond the standards for electronic devices and systems used in space and at accelerators," Ph.D. dissertation, Fac. Math. Sci., Univ. Jyväskylä, Jyväskylä, Finland, 2021, p. 88.